

See discussions, stats, and author profiles for this publication at: <https://www.researchgate.net/publication/230279736>

Description of the Morphology Dependent Charge Transport and Performance of Polymer:Fullerene Bulk Heterojunction Solar Cells

ARTICLE *in* ADVANCED FUNCTIONAL MATERIALS · JANUARY 2011

Impact Factor: 11.81 · DOI: 10.1002/adfm.201001515

CITATIONS

53

READS

40

5 AUTHORS, INCLUDING:



[Klara Maturova](#)

TNO

11 PUBLICATIONS 662 CITATIONS

SEE PROFILE



[Martijn Wienk](#)

Technische Universiteit Eindhoven

153 PUBLICATIONS 11,507 CITATIONS

SEE PROFILE



[Martijn Kemerink](#)

Linköping University

149 PUBLICATIONS 3,970 CITATIONS

SEE PROFILE

Description of the Morphology Dependent Charge Transport and Performance of Polymer:Fullerene Bulk Heterojunction Solar Cells

Klára Maturová, Svetlana S. van Bavel, Martijn M. Wienk, René A. J. Janssen, and Martijn Kemerink*

We present a combined numerical charge transport and morphology model to describe the current density–voltage (j – V) characteristics of three different, benchmark polymer:fullerene bulk heterojunction organic solar cells in which the device performance critically depends on the processing conditions or composition of the active layer. We find that an accurate description of the j – V characteristics over a broad bias range can be obtained when the actual complex, three-dimensional (3D) phase separation is represented by a simplified 2D or even 1D description. The morphological device model allows predicting the potential for increasing device performance by further optimizing the morphology. The optimal simplified morphology consists of two, relatively thin alternating vertically oriented slabs, that allow for fast lateral separation of photo-created holes and electrons. This morphology can effectively be described as 1D.

1. Introduction

Morphology and phase separation play an important role in the efficiency of organic bulk heterojunctions (OBHJ) solar cells.^[1] For optimizing the efficiency of a newly synthesized polymer in such a solar cell it is necessary to obtain control over the morphology of the active layer, usually via an empirical approach.^[2–10] Irrespective of the final outcome, it often remains uncertain whether further modification of the morphology might lead to higher efficiencies, as witnessed by numerous attempts to improve the morphology by, e.g., the choice of solvent, thermal annealing, solvent annealing, or using processing additives.^[1–10] Although qualitative rules of thumb have been established, a quantitative relation between morphology and device performance has so far been lacking. This paper describes a morphological device model that aims at making

a first step towards bridging that gap. It expands the results recently described for MDMO-PPV:PCBM (i.e. blends of poly[2-methyl-5-(3',7'-dimethyloctyloxy)-1,4-phenylene vinylene] and [6,6]-phenyl-C₆₁-butyric acid methyl ester)^[11] to other benchmark polymer:fullerene solar cells, processed into exceedingly different morphologies and thereby generalizes the approach.

The common picture of the operational principle of OBHJ solar cells is that a photo-generated exciton in, say, the donor phase diffuses to the interface with the nearby acceptor phase at which charge transfer takes place, i.e., an electron is transferred from the donor to the acceptor material. At

the interface free or weakly bound carriers can be separated and transported to the contacts through percolating paths in the different phases. All steps in this sequence of events are, directly or indirectly, affected by the morphology of the active layer. In our modeling, however, we limit ourselves on how charge transport and bimolecular charge recombination are affected by morphology and assume an effective rate for charge separation and geminate recombination. As a consequence, we focus on the relation between the largest length scales in the phase separated morphology of OBHJs and device characteristics, i.e., we will model length scales that are large as compared to single molecules or monomer units. Hence, a drift-diffusion model for charge transport can be applied. The model, which will be outlined below, uses material parameters like electron and hole mobilities, and generation and recombination rates as input. By treating these experimentally accessible quantities as effective parameters, the obvious fact that they are affected by the molecular scale morphology is implicitly incorporated, but not an outcome of our model.

The type of phase separation in OBHJ layers obtained by solution casting of conjugated polymers mixed with fullerene derivatives distinctly depends on the nature of the two components. Many polymer:fullerene blends, however, do show distinct similarities. Often, for small or intermediate amounts of fullerene material, sometimes even up to about 50 wt.%, a mixed polymer:fullerene phase is obtained in which larger scale phase (>10 nm) separation has not yet occurred. Solar cells that have such a well-mixed blend as the only phase in the active layer usually have a low efficiency.^[3] Larger amounts

Dr. K. Maturová, Dr. M. M. Wienk, Prof. R. A. J. Janssen, Dr. M. Kemerink
Molecular Materials and Nanosystems
Eindhoven University of Technology
P.O. Box 513, 5600 MB Eindhoven, The Netherlands
E-mail: m.kemerink@tue.nl

Dr. S. S. van Bavel
Laboratory of Materials and Interface Chemistry
Eindhoven University of Technology
P.O. Box 513, NL-5600 MB Eindhoven, The Netherlands

DOI: 10.1002/adfm.201001515

of fullerene (>50 wt.%) typically result in a phase-separated morphology. Of the two phases that are found, one is still the 'mixed' phase, consisting of both the polymer and the fullerene, while the second is an almost pure phase of crystalline fullerene material.^[3,12,13] The crystallization of fullerene material from the blend is an important driving force for the phase separation between the fullerene and the – usually amorphous – polymer. The efficiency of these phase-separated blends in solar cells can be much higher than for the homogeneously mixed layers, but the actual value can still vary dramatically. The classical example of this morphology is the one found in MDMO-PPV:PCBM, but it is often encountered for blends based on conjugated polymers with a low tendency to aggregate or crystallize. In selected examples, e.g. poly(3-hexylthiophene) (P3HT), the polymer has a profound tendency to crystallize and this then causes the domains of rather pure polymer to be formed, in addition to mixed and crystalline fullerene phases.^[5,14–16] For most blends, thermal or solvent annealing often results in enhanced phase separation with time. For blends that are initially intimately mixed (e.g. P3HT:PCBM) this results in an increased efficiency, but for blends where larger fullerene clusters are already present, thermal annealing is often detrimental.

Since the absorption coefficient in the visible range of the conjugated polymer is much higher than that of the fullerene, light absorption and charge generation predominantly take place in the mixed phase and – when present – in the pure polymer phase. Since the electron mobility in the semi-crystalline fullerene rich phase is orders of magnitude higher than in the mixed phase,^[17,18] the fullerene rich clusters are significant for electron transport, provided the photogenerated electron manages to travel from the mixed or pure polymer phase to the fullerene rich cluster.^[11,19]

In this paper we present the results obtained using a numerical model that describes the charge transport in OBHJ solar cells in relation to simplified 2D representations of the actual morphologies. It is a first attempt to quantitatively relate morphology to device characteristics for a broad range of materials in a single model. Current density–voltage (j – V) and current density–incident light power (j –ILP) curves have been calculated and are compared to experimental data for various polymer:fullerene blends processed under different conditions.^[11] It will be shown that the model can relate the large differences in device characteristics to differences in morphology as observed by transmission electron microscopy (TEM), atomic force microscopy (AFM), and scanning tunneling microscopy (STM). The fullerene used in this study is PCBM. Three prototypical polymers, regioregular P3HT (from Rieke Metals (R) and from Plextronics (P)), PF10TBT (poly[2,7-(9,9-didicylfluorene)-alt-5,5-(4',7'-di-2-thienyl-2',1',3'-benzothiadiazole)]), and MDMO-PPV, have been used (Figure 1a). P3HT produces a rather fine phase separation when cast into a film from a mixture with PCBM from a low boiling solvent, which can be coarsened by thermal annealing. For polymer:PCBM weight ratios of 1:4, PF10TBT and MDMO-PPV, produce a relatively coarse phase separation of pure PCBM domains embedded in mixed polymer:PCBM matrix, as described above. For each of these OBHJ solar cells, the required electron and hole mobilities that are used as input parameters of the model can be taken from literature.^[17,18,20]

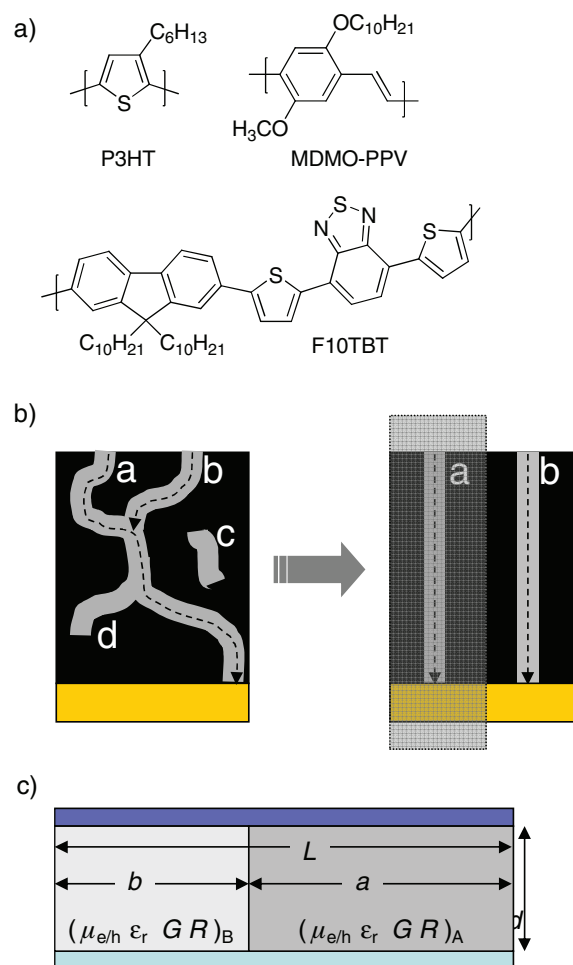


Figure 1. (a) Chemical structures of the three polymers used. Note that the $C_{10}H_{21}$ side chains are branched (linear) for MDMO-PPV (PF10TBT). (b) Mapping of the 'real' 3D morphology (left) on 2D (right). Isolated clusters, denoted 'c', and dead ends, denoted 'd', are ignored. Percolating pathways, 'a' and 'b', are straightened out. The gray box on the right indicates the repeat unit used in the calculations. (c) Simplified two-phase morphology with characteristic parameters used in the 2D drift-diffusion calculations.

Based on experimental TEM, AFM, and STM data of these blends, four simplified morphologies are proposed, that can accurately describe the differences in charge transport as a result of changing the morphology. This allows investigating whether the optimal morphology has been reached for a particular polymer:PCBM combination. Moreover, it allows predicting the performance of the device with an optimized (simplified) morphology. For MDMO-PPV:PCBM and P3HT:PCBM we find that very little improvement of the currently optimized cells (of given composition) may be expected from further fine tuning the morphology. However, the maximum output power of the PF10TBT:PCBM cell might be improved by ~25%.

2. Model

A numerical model was employed to perform simulations of j – V and j –ILP curves. The model employed has first been used

Table 1. List of parameters used in the simulations [a].

	P3HT(R):PCBM				PF10BT:PCBM			MDMO-PPV:PCBM			
	annealed		as cast		1:4		4:1	cb		t	
1D morphology	mixed phase	—	—	mixed phase	—	—	mixed phase	—	—	—	—
2D morphology	—	mixed phase	cryst. P3HT	—	mixed phase	PCBM cluster	—	mixed phase	PCBM cluster	mixed phase	PCBM cluster
ratio	—	11	9	—	4	16	—	5	15	5	15
L [nm]	—	40	—	—	100	—	—	40	—	800	—
d [nm]	100	100	100	100	210	200	—	80	—	140	—
G [nm ⁻³ s ⁻¹]	8.2	11	7	7	22.3	0	4.25	19.3	0	9.8	0
G_{eff} [nm ⁻³ s ⁻¹]	—	9.2	—	—	4.4	—	—	4.8	—	2.5	—
μ_h [m ² V ⁻¹ s ⁻¹]	5×10^{-8}	2×10^{-8}	4.5×10^{-8}	3.5×10^{-12}	4×10^{-8}	1×10^{-11}	8×10^{-9}	4×10^{-8}	2×10^{-11}	4×10^{-8}	2×10^{-11}
μ_e [m ² V ⁻¹ s ⁻¹]	3×10^{-7}	5×10^{-7}	2×10^{-11}	1.3×10^{-8}	2×10^{-10}	5×10^{-7}	3×10^{-7}	2×10^{-10}	3×10^{-7}	2×10^{-10}	3×10^{-7}
$\mu_{h,eff}$ [m ² V ⁻¹ s ⁻¹]	—	3×10^{-8}	—	—	8×10^{-9}	—	—	1×10^{-8}	—	1×10^{-8}	—
$\mu_{e,eff}$ [m ² V ⁻¹ s ⁻¹]	—	2.5×10^{-7}	—	—	3.8×10^{-7}	—	—	2.2×10^{-7}	—	2.2×10^{-7}	—
ϵ_r	3.6	3.6	3	3.9	3.6	3.9	3.9	3.6	3.9	3.6	3.9
g_0 [nm ⁻³]	0.3	0.3	0.3	0.3	0.3	0.3	0.3	0.3	0.3	0.3	0.3
HOMO [eV]	4.9	4.9	4.9	4.9	5.4	6.1	5.4	5.2	6.1	5.2	6.1
LUMO [eV]	4.1	4.1	2.7	4.1	4.1	4.1	4.1	4.1	4.1	4.1	4.1

[a] For all devices, the work function of the PEDOT:PSS bottom contact is $\chi_b = 5.1$ eV and of the LiF:Al top contact $\chi_t = 4.2$ eV.

in describing scanning Kelvin probe microscopy on OBHJs in light and dark and solves the coupled drift-diffusion, Poisson, and current continuity equations for holes and electrons on a rectangular 2D grid on which donor and acceptor phases are defined.^[21] The details of the model can be found in Ref. [21] and in the Supporting Information. The complex 3D morphology of the real OBHJ therefore has to be mapped onto a 2D description (Figure 1b, Figure 1c). The simplest, and for the present purposes sufficiently accurate, method is to represent the two phases (the mixed phase and the crystalline fullerene phase) as alternating slabs (Figure 1c). The width of the slabs is determined by two parameters: the size of the entire unit L , set equal to the typical fullerene cluster size plus the typical distance between two fullerene clusters, and the ratio between two phases. Each slab is, next to its geometry, characterized by the mobility $\mu_{e/h}$ of electrons and holes, the effective generation rate density G (in nm⁻³ s⁻¹) for free charges, the relative permittivity ϵ_r , the HOMO and LUMO energies which, in combination with the anode and cathode work functions, set the injection barriers for holes and electrons, and the density of states g_0 of the two phases. The entire sample has a uniform thickness d . The recombination rate is given by a modified Langevin expression $R = r_{pre}\gamma np$, where r_{pre} is the recombination prefactor, which is unity for pure Langevin recombination, γ is the Langevin rate constant,^[22] and n and p are the electron and hole charge densities. OBHJs which are not phase separated on a scale larger than ~10–20 nm are described by a 1D version of the model. In such a case the geometry is fully characterized by the active layer thickness, the mobility of electrons and holes in the single, mixed phase, the HOMO of the donor material and

the LUMO of the acceptor material, the average relative permittivity, the generation and recombination rates and the density of states. All parameters used are listed in Table 1.

The methodology described above to map the complex 3D morphology on 2D (Figure 1b) is clearly a strong simplification. Morphological details like dead ends, indicated by 'd', and isolated clusters, 'c', are not explicitly accounted for. Also the possibly meandering, variable width, or even fractal nature of the percolating pathways is only indirectly accounted for via the used effective mobility parameters. As such, the model should be regarded as a first order extension to totally homogeneous 1D drift-diffusion models that are commonly used in this field. The important addition of this extension is that it enables to distinguish between charge transport *within* a phase and *between* phases in a physically transparent manner. This is the basis of the outcomes of our model.

The approach followed separates the longest length scale of phase separation, i.e. beyond ~10–20 nm, from finer, molecular scale morphological details. The fact that this approach turns out to work quite well, as will be shown below, suggests that in the material systems studied these length scales are largely decoupled: finer molecular scale details can be captured in effective parameters as mobilities and charge generation rates that do not depend strongly on the long-range phase separation. The result that the magnitude of the mobility and the effective charge generation are local parameters can be understood by considering that these indeed strongly depend on the details of chain packing and the specific orientation of molecules at an interface, rather than on the extension of the phases beyond 10–20 nm.

In principle the employed methodology can be straightforwardly extended to account for concentration gradients, e.g. by introducing mobility gradients or variable cluster widths in the vertical direction. While such gradients have been reported to exist in few cases,^[16,23–26] there is still discussion on the sign of these gradients. We feel that inclusion of such phenomena is premature at this stage and would introduce rather arbitrary valued fitting parameters that do not lead to clear insights. The model also allows bilayers to be described,^[27] by setting the phase boundary horizontal instead of vertical.

The geometrical parameters are extracted from TEM, AFM, and STM images. Effective electron and hole mobilities were determined as geometrical averages: $\mu_{\text{eff}} = (\mu_A a + \mu_B b)/(a + b)$, where a and b are the widths of the mixed and crystalline phase and μ_A and μ_B measured mobilities in the blend and in the crystalline phase (Figure 1b).^[17,18,20] HOMO and LUMO energies are taken from Ref.[20,28,29]. The generation rate G_B is set zero in the weakly-absorbing pure PCBM phase, while in the strongly absorbing mixed phase G_A is determined from the effective generation rate $G_{\text{eff}} = (G_A a + G_B b)/(a + b)$, which has been extracted from the measured j - V curves as $G_{\text{eff}} = J_{\text{max}}/qd$, where J_{max} is the saturation current density measured under a high reverse bias (~ 10 V) under illumination representing an estimate for all charges generated in the blend, and q is the elementary charge. Following this procedure, the model is free of arbitrary valued fitting parameters since all parameters are known a priori within small margins reflecting the accuracy of their experimental determination.

3. Results

The morphology of the samples was investigated by combining TEM, AFM, and STM images as shown in Figure 2 for

P3HT(R):PCBM, PF10TBT:PCBM, and MDMO-PPV:PCBM. We propose a categorization of the observed morphology on basis of the degree of phase separation (see red contours in Figure 2) in Figure 3. On one extreme of this morphological scale, phase separation beyond ~ 10 – 20 nm is virtually absent. Of the studied samples, the as-cast P3HT(R):PCBM (Figure 2b) and 4:1 PF10TBT:PCBM (Figure 2d) OBHJ fall in this category (I). In both active layers no signs of phase separation on length scales in excess of a few nm can be observed in STM and TEM images. On the other extreme, long-range lateral phase separation is present. The MDMO-PPV:PCBM OBHJ spin-coated from toluene falls in this category (IV), as both AFM and TEM images (Figure 2f) show pronounced phase separation of PCBM clusters, several hundreds of nm in diameter, embedded in a mixed polymer:PCBM matrix. In between, we discern two intermediate morphologies with relatively fine phase separation. First, a category (II) of balanced phase separation in which both phases occur in approximately the same ratio. The annealed P3HT(R):PCBM (Figure 2a) OBHJ falls into this category. Electron tomography applied to P3HT:PCBM showed a three-dimensional network of crystalline P3HT fibers embedded in a mixed matrix.^[16] Second, a category (III) where the phase separation is still very fine, but one phase dominates over the other. MDMO-PPV:PCBM and PF10TBT:PCBM, both from chlorobenzene in weight ratio 1:4 fall in this category. The fibrous-looking network, which is most clearly visible in the TEM image for PF10TBT:PCBM (1:4) (Figure 2c) and in the AFM image for MDMO-PPV:PCBM (1:4, from chlorobenzene) (Figure 2e), consists of a polymer-rich phase that separates the fullerene clusters.

Below we will show that each category has its own characteristic features in the j - V curves. Reproducing the features of categories III and IV evidently requires the 2D model, whereas category I can be dealt with using a 1D model. The

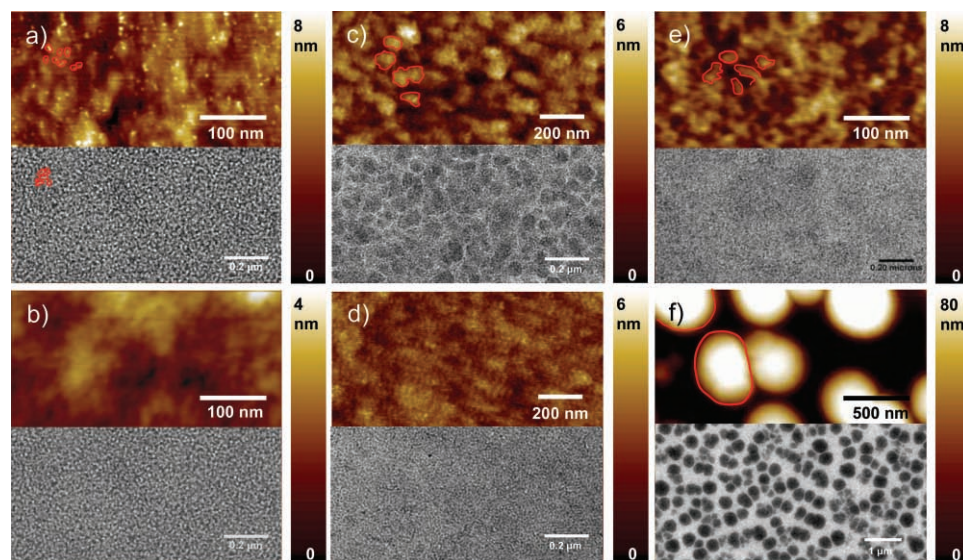


Figure 2. STM (a) and AFM (b–f) (top part of the figures) and TEM (bottom part) images of OBHJ active layers. (a,b) P3HT(R):PCBM, spin-coated from chlorobenzene and annealed at 130 °C for 10 min. (a) and untreated (b). (c,d) PF10TBT:PCBM in weight ratio 1:4 (c) and 4:1 (d) spin-coated from chlorobenzene. (e,f) MDMO-PPV:PCBM spin-coated from chlorobenzene at 1500 rpm (e) and toluene at 800 rpm (f). z-scale of AFM and STM images: 8 nm (a, e), 4 nm (b), 6 nm (c,d) and 80 nm (f). The red contours guide the eye to identify the phase separation that is present in panels a, c, e, and f.

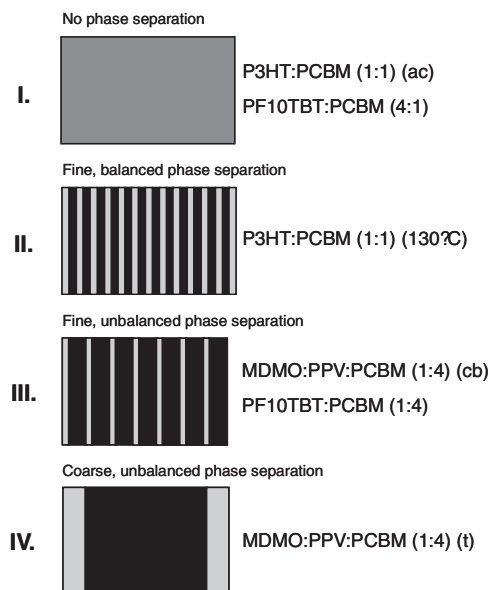


Figure 3. Schematic representation of polymer:PCBM blend morphologies as proposed on basis of TEM, AFM, and/or STM. The grey slabs represent the most polymer rich phase and black phase represent the most fullerene rich phase.

parameters used in the 2D simulation for thermally annealed P3HT(R):PCBM are shown in Table 1. In the 2D calculation narrow alternating slabs are considered. The first one consists of a mixed P3HT(R):PCBM phase, where $\mu_e > \mu_h$. The second phase consist of pure crystalline P3HT(R), where $\mu_e \ll \mu_h$. As P3HT absorbs most of the light, the generation rate in both the crystalline P3HT(R) and mixed P3HT(R):PCBM phases is nonzero. For the mixed phase electron transfer to the fullerene readily occurs after absorption of light by P3HT(R), but also for the pure P3HT(R) phase absorption of light contributes to charge generation. Surprisingly, we find that the outcomes of the 2D model for category II (fine and balanced phase separation) coincide with those of the 1D model provided that the (high) electron mobility of the acceptor phase and the (high) hole mobility of the donor phase are used (see inset of Figure 4). The fact that 1D and 2D coincide can be understood by considering the limiting situation of increasingly narrow stripes of donor and acceptor material, which should eventually behave as a 1D system. This finding rationalizes the previous successful use of 1D models for the P3HT:PCBM material system.^[18] In the following, we will use the less computationally demanding 1D model for this category.

It has been shown before that untreated P3HT:PCBM is well mixed and its efficiency can be improved by annealing above 100 °C. Thermal annealing results in an enhanced crystallinity of both the P3HT and PCBM phases and extended phase separation.^[5,15,30] The formation of the phase separated and more crystalline morphology by thermal annealing leads to a remarkable increase in the hole mobility by a factor $\sim 10^4$ and a lesser increase by $\sim 10^1$ in the electron mobility, see also Table 1.^[18] Although the photocurrents at -10 V are very similar and hence the free carrier generation rates are almost equal in the as-cast and annealed devices, the latter has a superior performance,

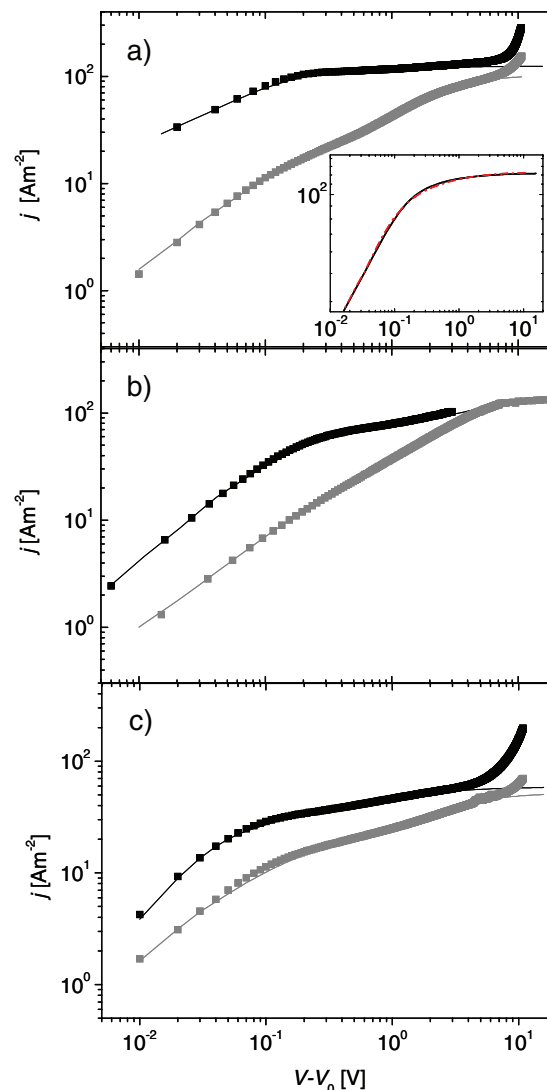


Figure 4. Measured (symbols) and simulated (lines) current vs. reduced bias $|V-V_{oc}|$ curves for polymer:fullerene bulk-heterojunction solar cells. The active layer consist of (a) P3HT(R):PCBM, spin-coated from chlorobenzene, annealed (black), untreated (grey), inset: solid line: 1D calculation, red dash-dotted line: 2D calculation; (b) PF10TBT:PCBM at weight ratio 1:4 (black) and 4:1 (grey); (c) MDMO-PPV:PCBM from chlorobenzene at 1500 rpm (black) and toluene at 800 rpm (grey). The sharp increase in measured current around 10 V is due to minority carrier injection.

as shown in Figure 4a. This difference is due to a far stronger bimolecular recombination in the as-cast device. Because G is determined experimentally from the current under illumination at large negative bias, geminate losses are effectively accounted for in the value of G as long as these are not field-dependent. The somewhat higher value of G in the annealed sample likely reflects a more efficient free charge generation or an increased absorption of light. The first explanation corroborates recent results where we have shown a positive correlation between charge generation and the onset of phase separation into larger domains.^[13,31] Further support for the dominant role of bimolecular recombination in the as-cast films comes

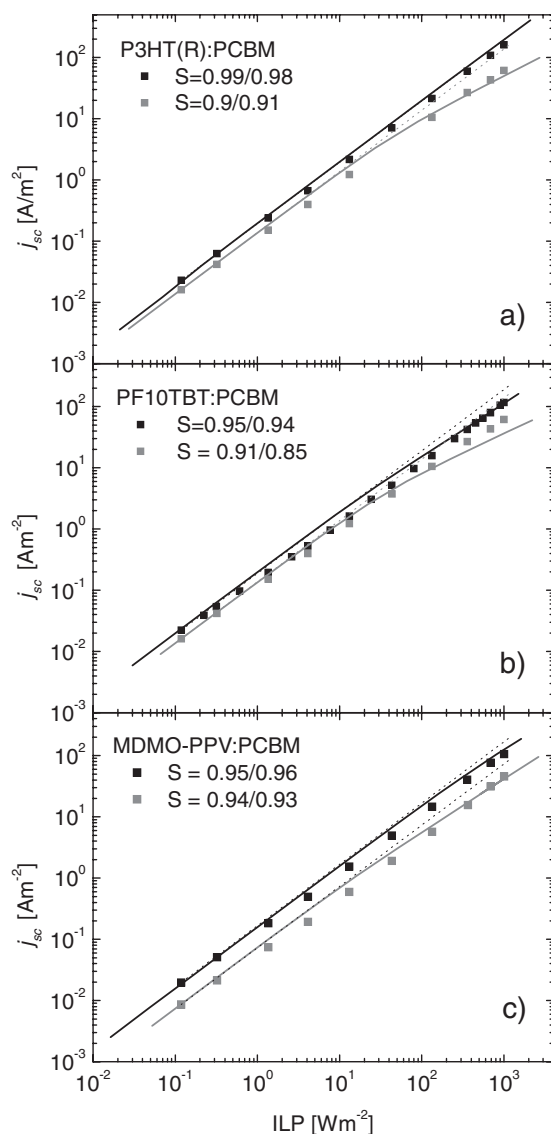


Figure 5. Measured (symbols) and simulated (lines) short circuit current density (j_{sc}) vs. incident light power (ILP) the polymer:fullerene bulk-heterojunction solar cells. (a) P3HT:PCBM, spin-coated from chlorobenzene, annealed (black), untreated (grey); (b) PF10TBT:PCBM at weight ratio 1:4 (black) and 4:1 (grey); (c) MDMO-PPV:PCBM from chlorobenzene at 1500 rpm (black) and toluene at 800 rpm (grey). In the simulations, the ILP is changed by changing the generation rate G in the absorbing phase. The parameters S refer to the slope of j_{sc} vs. ILP as $j_{sc} \sim \text{ILP}^S$ in experimental and calculated curves, respectively. S is determined by a least squares fit over the entire ILP range. The dotted lines indicate unity slope.

from the light intensity dependence of the short-circuit current shown in Figure 5a. In this logarithmic plot the short-circuit current of the annealed P3HT:PCBM device shows a slope that is extremely close to unity for the entire range of ILP ($j_{sc} \sim \text{ILP}^S$, with $S \approx 1$), indicative of very low bimolecular recombination. For the as-cast device, in contrast, j_{sc} shows a slope that drops below unity at rather low light levels, indicating bimolecular recombination. The main reason for the different behavior of the two devices is the more crystalline nature of P3HT(R) in the

annealed device and the associated increased hole mobility that enables efficient transport of photocreated holes.

Qualitative comparison of the j - V curves of MDMO-PPV:PCBM devices in categories III and IV with the P3HT:PCBM devices in I and II reveals two major differences. First, substantial performance differences are present between devices with identical electron and hole mobilities, c.f. the chlorobenzene and toluene cast devices in Table 1. Second, an almost linear slope (on double-log scale) is observed at intermediate bias, 0.1–1 V in Figure 4c. Both features can directly be related to the 2D phase separated morphology, and were extensively discussed in a previous paper.^[11] In devices with this morphology, losses to bimolecular recombination are avoided when electrons, which are photocreated in the mixed phase, are transported to the electron extracting top contact via the PCBM clusters where the electron mobility is about three orders of magnitude higher than in the mixed phase. Since these clusters are finer spaced in the chlorobenzene-cast device than in the toluene-cast cell, the former OBHJ is more efficient. The larger role of bimolecular recombination in the latter device is reflected in the light intensity dependence shown in Figure 5c showing a small but systematic difference in slope S , with lower values of S , indicating higher bimolecular recombination, for the coarser, toluene-cast sample.

The linear slope (on double-log scale) in the j - V curve can now be identified as being due to a transition between two regimes. At low electric fields, as discussed above, electrons make a lateral motion to the PCBM clusters. At very high fields, here above a few Volts over ~ 100 nm, the shorter transit time and the changed field distribution prevent this path and electrons remain in the mixed phase where they are exposed to recombination. The 'linear' part is the transition between these two regimes.^[11] It can therefore be used as an experimentally easily obtained indicator for 2D-like charge transport.

In view of the preceding discussion, it is to be expected that the PF10TBT:PCBM blend in weight ratio 4:1, which shows no measurable phase separation, can be well described by the 1D model. Moreover, the low electron and hole mobilities should lead to j - V and j -ILP curves that resemble those of the as-cast P3HT:PCBM, which has comparably low mobilities. The higher hole and lower electron mobility in the PF10TBT:PCBM system is likely the consequence of the higher polymer:PCBM ratio. Indeed, the 4:1 PF10TBT:PCBM device behaves quite similar to the as-cast P3HT:PCBM device, c.f. the grey curves in Figure 4b, Figure 4a and in Figure 5b, Figure 5a. The large voltage range over which the extracted current density increases and the resulting low short circuit current reflect the long, as compared to the recombination rate, transit time of the charge carriers due to their low mobility. Only at very high voltages does the transit time become substantially shorter than the recombination lifetime and does the device current saturate.

In contrast, the parameters and morphology of the 1:4 PF10TBT:PCBM device are very similar to those of the chlorobenzene-cast MDMO-PPV:PCBM device, the main differences being the somewhat longer length scale of phase separation and higher generation rate in the former – see Table 1. Hence, similar behavior is expected and indeed observed; see the black curves in Figure 4b, Figure 4c and Figure 5b, Figure 5c. The different (reduced) bias at which the transition

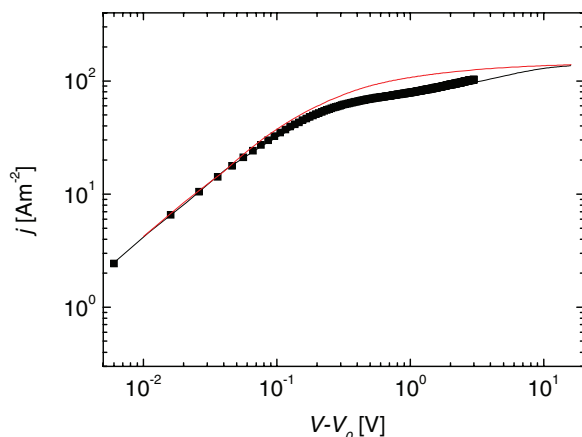


Figure 6. Measured (symbols) and simulated (lines) j - V curves of a PF10TBT:PCBM (1:4) bulk-heterojunction solar cell with the actual phase separation ($L \sim 100$ nm) (black). The red line is a prediction for the same device with optimized, finer phase separation ($L = 40$ nm).

from low to high-field behavior sets in is the result of the differences mentioned above.

From the analysis of the three polymer:PCBM systems presented above, it follows that the optimal long-range morphology of this type of OBHJ is the one schematically represented in Figure 3 as category II, i.e. a very fine (lateral) alternation of electron and hole transporting layers. This can also be achieved by a purely 1D morphology represented by category I, provided that electron and hole mobilities are high.

The annealed P3HT:PCBM OBHJ has the optimal morphology of category II, and consequently the lowest bimolecular recombination, i.e., highest S parameter (Figure 5a) of the devices studied. The morphology of the MDMO-PPV:PCBM OBHJ from chlorobenzene is close to category II, and further refinement of the morphology only leads to marginal improvements in performance.^[32] More interesting in this respect is the 1:4 PF10TBT:PCBM device which can, in principle, be significantly improved. In case the total width of the mixed phase plus PCBM cluster, L , could be shrunk down from 100 nm to 40 nm, like for MDMO-PPV:PCBM OBHJ from chlorobenzene, while maintaining all other parameters the red line in Figure 6 is obtained. In that case, j_{sc} can increase from 80 to 110 $A m^{-2}$. It is important to note that the characteristic linear slope at intermediate bias has disappeared in the optimized device. Hence, in line with the preceding discussion, this feature can be identified as an indicator of a non-optimal morphology.

A more detailed comparison of performance indicators of the devices studied can be found in Table 2. It shows that the maximum output power of the PF10TBT:PCBM OBHJ with fine phase separation increases from 40 $W m^{-2}$ (feature size ~ 100 nm) to 52 $W m^{-2}$ (feature size ~ 30 nm) and exceeds the maximum output power of annealed P3HT:PCBM.

For P3HT:PCBM solar cells the morphology can vary significantly with the particular type of P3HT used. To assess the effect of different batches with different morphologies, we have compared the performance of P3HT(R):PCBM and P3HT(P):PCBM OBHJ solar cells after annealing. The bright field (BF) TEM images of these two layers (Figure 7a, Figure 7b)

Table 2. Characteristics of solar cells in Figure 4 and 6.

	V_{oc} [V]	J_{sc} [$A m^{-2}$]	MPP [$W m^{-2}$]	FF
P3HT(R):PCBM (as cast)	0.7	-36	9	0.36
P3HT(R):PCBM (annealed)	0.59	-113	40	0.59
PF10TBT:PCBM 4:1	1.07	-39	13	0.32
PF10TBT:PCBM 1:4	1.01	-79	40	0.50
MDMO-PPV:PCBM (toluene)	0.83	-24	9	0.46
MDMO-PPV:PCBM (chlorobenzene)	0.85	-45	21	0.55
PF10TBT:PCBM 1:4 (improved) [a]	1.01	-107	52	0.48

[a] calculated

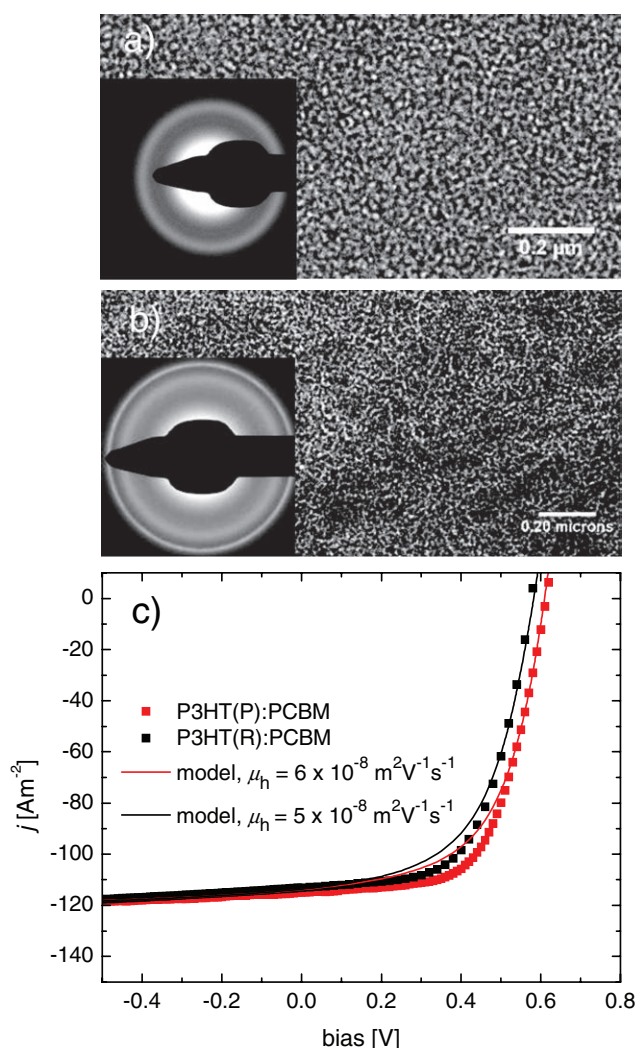


Figure 7. (a) BF TEM image of an annealed (130 °C for 10 min) P3HT(R):PCBM layer. (b) BF TEM image of an annealed (130 °C for 20 min) P3HT(P):PCBM active layer. The insets show the corresponding electron diffraction patterns. (c) Experimental (symbols) j - V curves and corresponding 1D model calculations (lines) for P3HT(R):PCBM and P3HT(P):PCBM OBHJs.

differ significantly. For P3HT(P):PCBM (panel b) a fibrous network of crystalline P3HT whiskers is clearly visible in BF-TEM but not for P3HT(R):PCBM, demonstrating that the morphology of the two layers are significantly dissimilar. We note, however, that the apparent absence of fibers in the BF-TEM images of P3HT(R):PCBM does not imply that they are completely absent in the film. In fact, by 3D electron tomography, a dense 3D network of P3HT nanowires in the whole volume of P3HT(R):PCBM films has been visualized due to improved contrast in the 3D datasets as compared with BF images.^[33] Despite the differences in morphology, the j - V characteristics of both P3HT:PCBM films are similar, with the P3HT(P) batch performing slightly better than P3HT(R) (P/R: V_{oc} = 0.61/0.59 V; J_{sc} = 115/113 A m⁻²; fill factor = 0.62/0.59, MPP = 43/40 W m⁻²) (Figure 7c). The best 1D model calculations for these devices only differed in the used hole mobility; μ_h = $6 \times 10^{-8}/5 \times 10^{-8}$ m² V⁻¹ s⁻¹. We should remark that for both calculations the fill factor does not fully correspond to the experiment, suggesting a somewhat weaker bimolecular recombination in the actual devices, than used in the calculation.

As a last remark we should come back to the surprising fact that the very simplified morphology used in the calculations presented here seems to catch the most relevant features of the j - V and j -ILP curves of three benchmark polymer:fullerene bulk heterojunction solar cells. In particular, in the annealed P3HT:PCBM system the actual morphology, where the random nanoscale network of crystalline P3HT is embedded in the mixed phase matrix not quite resembles alternating slabs.^[16] Apparently the randomness does not prevent the system from behaving 1D-like. One can speculate that a morphology with only vertical fibers would give a higher effective hole mobility and a (marginally) better performance. Something similar holds for the 1:4 PF10TBT:PCBM device, where we cannot be sure that the PCBM clusters run as vertical columns through the device. Still it is reasonable to distinguish transport within a phase and between phases, which is the basis of the outcomes of our model. As stated in the introduction, finer morphological details like dead ends, isolated clusters and molecular packing and mixing are not explicitly accounted for, and it remains an interesting question how the molecular scale morphology translates into the effective parameters used here.^[22,34,35] In particular, it may shed light on the reasons as to why a reduced Langevin prefactor (r_{pre} = 0.1)^[22,36] needs to be used for the P3HT:PCBM system in order to reproduce the fill factor.

4. Conclusions

We have presented a numerical charge transport and morphology model that reproduces the key features of the electrical characteristics of prototypical polymer:fullerene bulk heterojunction solar cells under illumination. The morphological model we use specifically addressed lengths scales that are larger than ~10–20 nm that are relevant for charge transport and bimolecular recombination. Shorter, e.g. molecular, length scales that are important for charge generation, geminate recombination, and charge carrier mobility are not explicitly taken into account and their effect is accounted for by using experimentally determined charge generation rates and mobilities. On this

basis, we distinguish four qualitatively different simplified morphologies that have been used to accurately describe the j - V and j -ILP characteristics of six different blends involving mixtures of three well known conjugated polymers with PCBM. For best performance, the OBHJ should have a phase separated morphology with feature sizes that are smaller than ~50 nm. Such fine phase separated morphology improves charge transport within and between the two phases and reduces bimolecular charge recombination. Moreover, the characteristic sublinear slope that is sometimes observed at intermediate bias in the double log plot of the current density versus reduced bias is identified as indicative of a non-optimal morphology.

5. Experimental Section

Three different polymers were used as donor material: regioregular P3HT, PF10TBT, and MDMO-PPV were mixed in solution with PCBM as accepting material. Films were deposited by spin coating on top of PEDOT:PSS (HC Starck, Clevis P VP Al 4083)/ITO/glass substrates. Each of the three blends was prepared or processed in two different ways, leading to a solar cell with a high and a low efficiency. The standard P3HT:PCBM (weight ratio 1:1, 10 mg ml⁻¹ P3HT) solar cell was spin-coated from chlorobenzene at 1500 rpm. The P3HT(R) (Rieke Metals Inc.) used had M_n = 50000 g mol⁻¹, PDI = 2.14 and regioregularity exceeding 98.5% as determined by NMR. The high efficiency device was obtained by annealing at 130 °C for 10 min. The low efficiency device was not thermally processed and measured as cast. For comparison, a different batch of P3HT(P) (Plextronics, Inc., M_n = 19400 g mol⁻¹, PDI = 1.4, and regioregularity 98% as described previously^[16]) was used to make P3HT(P):PCBM layers. The layers were spin cast from 1,2-dichlorobenzene (ODCB) (weight ratio 1:1, 10 mg ml⁻¹ P3HT) followed by a 20 min. thermal annealing at 130 °C. PF10TBT (M_n = 9600 g mol⁻¹, PDI = 3.6):PCBM (4 mg ml⁻¹) layers were spin-coated from chlorobenzene in weight ratios 1:4 (high efficiency) and 4:1 (low efficiency) at 1500 rpm. The MDMO-PPV (M_n = 124000 g mol⁻¹, PDI = 5.0):PCBM (weight ratio 1:4) solar cell was spin-coated from chlorobenzene (high efficiency) and toluene (low efficiency) at 1500 and 800 rpm, respectively.

After deposition of the active layers, the substrates were immediately transferred to an N₂-filled glovebox ([H₂O], [O₂] < 1 ppm) for deposition of the top contact (~1 nm LiF followed by ~100 nm Al) by thermal evaporation in high vacuum (<10⁻⁶ mbar). j - V characteristics were taken at room temperature inside the glove box using a Keithley 2400 SMU, either in the dark or under white light illumination with UV (CG 385) and infrared (KG1) filtered light from an tungsten halogen lamp with a maximum estimated light output of 1000 W m⁻². The currents reported were not corrected for spectral mismatch. Incident light power (ILP) was varied using a calibrated set of neutral density filters.

The morphology of the active layers was characterized using TEM, AFM, and STM. For TEM-investigation, the active layers were floated onto the surface of demineralized water and picked up with 400-mesh copper TEM grids. The bright-field TEM images were obtained with a Tecnai G² 20 (FEI Co., the Netherlands) operated at 200 kV. AFM images were taken in tapping mode using a Veeco MultiMode AFM connected to an extended NanoScope IV controller and NanoSensors tips (PPP-NCHR, k ~ 40 N m⁻¹). STM was measured with a Veeco MultiMode in STM mode connected to an RHK SPM100 controller using cut PtIr tips. All STM and AFM experiments were performed in the N₂-filled glovebox.

Supporting Information

Supporting Information is available from the Wiley Online Library or from the author.

Acknowledgements

The work of K.M. is made possible by a NanoNed grant (NanoNed is the Dutch nanotechnology initiative by the Ministry of Economic Affairs). The work of S.S.v.B. forms part of the research program of the Dutch Polymer Institute (DPI), project 524.

Received: July 23, 2010

Published online: November 9, 2010

-
- [1] X. Yang, J. Loos, *Macromolecules* **2007**, *40*, 1353.
- [2] S. E. Shaheen, C. J. Brabec, N. S. Sariciftci, F. Padinger, T. Fromherz, J. C. Hummelen, *Appl. Phys. Lett.* **2001**, *78*, 841.
- [3] J. K. J. van Duren, X. Yang, J. Loos, C. W. T. Bulle-Lieuwma, A. B. Sieval, J. C. Hummelen, R. A. J. Janssen, *Adv. Funct. Mater.* **2004**, *14*, 425.
- [4] F. Padinger, R. Rittberger, N. S. Sariciftci, *Adv. Funct. Mater.* **2003**, *13*, 85.
- [5] X. Yang, J. Loos, S. C. Veenstra, W. J. H. Verhees, M. M. Wienk, J. M. Kroon, M. A. J. Michels, R. A. J. Janssen, *Nano Lett.* **2005**, *5*, 579.
- [6] G. Li, V. Shrotriya, J. Huang, Y. Yao, T. Moriarty, K. Emery, Y. Yang, *Nat. Mater.* **2005**, *4*, 864.
- [7] W. Ma, C. Yang, X. Gong, K. Lee, A. J. Heeger, *Adv. Funct. Mater.* **2005**, *15*, 1617.
- [8] J. Peet, J. Y. Kim, E. Coates, W. L. Ma, D. Moses, A. J. Heeger, G. C. Bazan, *Nat. Mater.* **2007**, *6*, 497.
- [9] J. K. Lee, W. L. Ma, C. J. Brabec, J. Yuen, J. S. Moon, J. Y. Kim, K. Lee, G. C. Bazan, A. J. Heeger, *J. Amer. Chem. Soc.* **2008**, *130*, 3619.
- [10] M. M. Wienk, M. Turbiez, J. Gilot, R. A. J. Janssen, *Adv. Mater.* **2008**, *20*, 2556.
- [11] K. Maturova, S. S. van Bavel, M. M. Wienk, R. A. J. Janssen, M. Kemerink, *Nano Lett.* **2009**, *9*, 3032.
- [12] H. Hoppe, M. Niggemann, C. Winder, J. Kraut, R. Hiesgen, A. Hinsch, D. Meissner, N. S. Sariciftci, *Adv. Funct. Mater.* **2004**, *14*, 1005.
- [13] D. Veldman, O. Ipek, S. C. J. Meskers, J. Sweelssen, M. M. Koetse, S. C. Veenstra, J. M. Kroon, S. S. van Bavel, J. Loos, R. A. J. Janssen, *J. Am. Chem. Soc.* **2008**, *130*, 7721.
- [14] T. Erb, U. Zhokhavets, G. Gobsch, S. Raleva, B. Stuhn, P. Schilinsky, C. Waldauf, C. J. Brabec, *Adv. Funct. Mater.* **2005**, *15*, 11936.
- [15] Y.-C. Huang, Y.-C. Liao, S.-S. Li, M.-C. Wu, C.-W. Chen, W.-F. Su, *Sol. Energy Mater. Sol. Cells* **2009**, *93*, 888.
- [16] S. S. van Bavel, Erwan Sourty, G. de With, J. Loos, *Nano Lett.* **2009**, *9*, 507.
- [17] V. D. Mihailetchi, L. J. A. Koster, P. W. M. Blom, C. Melzer, B. de Boer, J. K. J. van Duren, R. A. J. Janssen, *Adv. Funct. Mater.* **2005**, *15*, 795.
- [18] V. D. Mihailetchi, H. Xie, B. de Boer, L. J. A. Koster, P. W. M. Blom, *Adv. Funct. Mater.* **2006**, *16*, 699.
- [19] W. Geens, T. Martens, J. Poortmans, T. Aernouts, J. Manca, L. Lutsen, P. Heremans, S. Borghs, R. Mertens, D. Vanderzande, *Thin Solid Films* **2004**, *451–452*, 498.
- [20] D. J. D. Moet, L. H. Slooff, J. M. Kroon, S. S. Chevtchenko, J. Loos, M. M. Koetse, J. Sweelssen, S. C. Veenstra, *Mater. Res. Soc. Symp. Proc.* **2007**, *974*, CC03.
- [21] K. Maturova, M. Kemerink, M. M. Wienk, D. S. H. Charrier, R. A. J. Janssen, *Adv. Funct. Mater.* **2009**, *19*, 1379.
- [22] C. Groves, N. C. Greenham, *Phys. Rev. B* **2008**, *78*, 155205-1.
- [23] M. Campoy-Quiles, T. Ferenczi, T. Agostinelli, P. G. Etchegoin, Y. Kim, T. D. Anthopoulos, P. N. Stravrinou, D. C. Bradley, J. Nelson, *Nat. Mater.* **2007**, *7*, 158.
- [24] C. M. Björström Svanström, J. Rysz, A. Bernasik, A. Budkowski, F. Zhang, O. Inganäs, M. R. Andersson, K. O. Magnusson, J. J. Benson-Smith, J. Nelson, E. Moons, *Adv. Mater.* **2009**, *21*, 4398.
- [25] B.-Y. Yu, W.-C. Lin, W.-B. Wang, S.-I. Iida, S.-Z. Chen, C.-Y. Liu, C.-H. Kuo, S.-H. Lee, W.-L. Kao, G.-J. Yen, Y.-W. You, C.-P. Liu, J.-H. Jou, J.-J. Shyue, *ACS Nano* **2010**, *4*, 833.
- [26] Z. Xu, L.-M. Chen, G. Yang, C.-H. Huang, J. Hou, Y. Wu, G. Li, C.-S. Hsu, Y. Yang, *Adv. Funct. Mater.* **2009**, *19*, 1227.
- [27] L. Ayzner, C. J. Tassone, S. H. Tolbert, B. J. Schwartz, *J. Phys. Chem. C* **2009**, *113*, 20050.
- [28] M. Al-Ibrahim, H. K. Roth, U. Zhokhavets, G. Gobsch, S. Sensfuss, *Sol. Energy Mater. Sol. Cells* **2005**, *85*, 13.
- [29] V. D. Mihailetchi, P. W. M. Blom, J. C. Hummelen, M. T. Rispens, *J. Appl. Phys.* **2003**, *94*, 6849.
- [30] Swinnen, I. Haeldermans, M. vande Ven, J. D'Haen, G. Vanhoyland, S. Aresu, M. D'Olieslaeger, J. Manca, *Adv. Funct. Mater.* **2006**, *16*, 760.
- [31] D. Di Nuzzo, A. Aguirre, M. Shahid, V. S. Gevaerts, S. C. J. Meskers, R. A. J. Janssen, *Adv. Mater.* **2010**, DOI: 10.1002/adma.201001452.
- [32] K. Maturova, R. A. J. Janssen, M. Kemerink, *ASC Nano* **2010**, *4*, 1385.
- [33] S. S. van Bavel, M. Bärenklau, G. de With, H. Hoppe, J. Loos, *Adv. Funct. Mater.* **2010**, *20*, 1458.
- [34] B. Walker, *Proc. IEEE* **2009**, *97*, 1587.
- [35] P. Peumans, S. R. Forrest, *Chem. Phys. Lett.* **2004**, *358*, 27.
- [36] L. J. A. Koster, V. D. Mihailetchi, P. W. M. Blom, *Appl. Phys. Lett.* **2006**, *88*, 052104-1.